

2001-2022 global gross primary productivity dataset using an ensemble model based on random forest

Xin Chen¹, Tiexi Chen^{1,2,3*}, Xiaodong Li⁴, Yuanfang Chai⁵, Shengjie Zhou¹, Renjie Guo⁶, Jie Dai¹

¹School of Geographical Sciences, Nanjing University of Information Science and Technology, Nanjing 210044, Jiangsu, China.

²Qinghai Provincial Key Laboratory of Plateau Climate Change and Corresponding Ecological and Environmental Effects, Qinghai University of Science and Technology, Xining 810016, China

³School of Geographical Sciences, Qinghai Normal University, Xining 810008, Qinghai, China.

⁴Qinghai Institute of Meteorological Science, Xining 810008, Qinghai, China.

⁵Department of Earth Sciences, Vrije Universiteit Amsterdam, Boelelaan 1085, 1081 HV, Amsterdam, the Netherlands

⁶Faculty of Geographical Science, Beijing Normal University, Beijing, China.

Correspondence to: Tiexi Chen (txchen@nuist.edu.cn)

Abstract. Advancements in remote sensing technology have significantly contributed to the improvement of models for estimating terrestrial gross primary productivity (GPP). However, discrepancies in spatial distribution and interannual variability within GPP datasets pose challenges to a comprehensive understanding of the terrestrial carbon cycle. In contrast to previous models that rely on remote sensing and environmental variables, we developed an ensemble model based on random forest (ERF model). This model used the GPP outputs of established models (EC-LUE, GPP-kNDVI, GPP-NIRv, Revised-EC-LUE, VPM, MODIS) as input to estimate GPP. The ERF model demonstrated superior, explaining 85.1% of the monthly GPP variations at 170 sites and surpassing the performance of both selected GPP models (67.7%-77.5%) and an independent random forest model using remote sensing and environmental variables (81.5%). Additionally, the ERF model improved the accuracy across each month and various subvalues, mitigating the issue of "high value underestimation and low value overestimation" in GPP estimates. Over the period from 2001 to 2022, the global GPP estimated by the ERF model was 132.7 PgC yr⁻¹, with an increasing trend of 0.42 PgC yr⁻², which is comparable to or slightly better than the accuracy of other mainstream GPP datasets in term of validation results from ChinaFlux. In summary, the ERF model offers a reliable alternative for reducing uncertainties in GPP estimate, providing a more dependable global GPP estimate.

1 Introduction

Gross primary productivity (GPP) is the largest carbon flux in the global carbon cycle, and serves as the primary input of carbon into the terrestrial carbon cycle. Uncertainties in GPP estimates can propagated to other carbon flux estimates, making

33 it crucial to clarify the spatio-temporal patterns of GPP (Xiao et al., 2019; Ruehr et al., 2023). However, global GPP is variously
34 estimated from 90 PgC yr⁻¹ to 160 PgC yr⁻¹ across different studies, with these variations becoming more pronounced when
35 scaled down to regional scales or specific ecosystem types. This variability underscores the necessity for innovative methods
36 to reduce the uncertainty in GPP estimates (Jung et al., 2019; Ryu et al., 2019; Anav et al., 2015).

37 The light use efficiency (LUE) model is one of the most widely adopted methods for estimating GPP. It assumes that GPP is
38 proportional to the photosynthetically active radiation absorbed by vegetation, and optimizes the spatio-temporal pattern of
39 GPP through meteorological constraints such as temperature and water (Pei et al., 2022). However, variations in these
40 constraints varies significantly, leading to differences of over 10% in model explanatory power. (Yuan et al., 2014). Recent
41 studies have proposed some novel vegetation indices that have been shown to be effective proxies for GPP through theoretical
42 derivation and observed validation (Badgley et al., 2017; Camps-Valls et al., 2021). However, these vegetation indices often
43 use only remote sensing data as an input for estimating long-term GPP without considering meteorological factors, which has
44 led to some controversy (Chen et al., 2024; Dechant et al., 2020; Dechant et al., 2022). Both LUE and vegetation index models
45 use a combination of linear mathematical formulas to estimate GPP. However, ecosystems are inherently complex, and the
46 biases introduced by these numerical models increase the uncertainty in the estimates of the final product (GPP). Machine
47 learning models has shown great potential for improving GPP estimates in previous studies (Jung et al., 2020; Guo et al., 2023).
48 These model are trained by non-physical means directly using GPP observations and selected environmental and vegetation
49 variables, and the performance of the model depends on the number and quality of observed data and the representativeness
50 of input data. Nevertheless, direct validation from flux towers of FLUXNET reveals that these models typically explain only
51 about 70% of monthly GPP variations, with similar performance to other GPP models (Wang et al., 2021; Badgley et al., 2019;
52 Zheng et al., 2020; Jung et al., 2020). Due to deviations in the model structure, a common limitation across these models is
53 poor estimate of monthly extreme GPP, leading to the phenomenon of "high value overestimation and low value
54 overestimation" (Zheng et al., 2020). Especially for extremely high values, which usually occur during the growing season and
55 largely determine the annual value and interannual fluctuations of GPP, this underestimation may hinder our understanding of
56 the global carbon cycle.

57 It is challenging for a single model to provide accurate estimates for all global regions. Ensemble models have been shown to
58 outperform single models in previous studies, potentially addressing some inherent issues in model estimate (Chen et al., 2020;
59 Yao et al., 2014). Traditional multi-model ensemble methods usually use simple multi-model average or a weighted bayesian
60 average. However, these methods typically assign fixed weights to each model and are essentially linear combinations. Recent
61 studies have applied machine learning methods to multi-model ensembles to establish nonlinear relationships between multiple
62 simulated target variables and real target variable, improving simulation performance (Bai et al., 2021; Yao et al., 2017; Tian
63 et al., 2023). Whether this method can improve some common problems with a single GPP model, such as high value
64 underestimation and low value overestimation, is not clear and needs to further investigation.

65 In this study, we attempt to use an ensemble model based on the random forest (ERF model) to improve global GPP estimate.
66 Specifically, the work of this study includes the following: (1) Recalibrating the parameters for each model, and comparing

67 the performance of six GPP models and the ERF model; (2) Focusing on the phenomenon of “high value underestimation and
68 low value overestimation” in each model, and evaluating the performance of each model in different months, vegetation types
69 and subvalues (high value, median value, low value); (3) Developing a global GPP dataset using the ERF model and validate
70 its generalization using GPP observations from ChinaFlux.

71 2 Method

72 2.1 Data at the global scale

73 In this study, we selected remote sensing data from the Moderate Resolution Imaging Spectroradiometer (MODIS) and
74 meteorological data from ERA5 to estimate global GPP (Hersbach et al., 2020). For the remote sensing data, surface reflectance
75 (red band, near infrared band, blue band and shortwave infrared band), leaf area index (LAI) and fraction of photosynthetically
76 active radiation (FPAR) were used. For meteorological data, we selected average air temperature, dew point temperature,
77 minimum air temperature, total solar radiation and direct solar radiation. Dew point temperature and air temperature were used
78 to calculate saturated vapor pressure difference (VPD) (Yuan et al., 2019), and diffuse solar radiation was derived as the
79 difference between total solar radiation and direct solar radiation. Minimum air temperature was obtained from the hourly air
80 temperature. CO₂ data were obtained from the monthly average carbon dioxide levels measured by the Mauna Loa Observatory
81 in Hawaii. Table 1 provides an overview of the datasets used in this study.

82

83 **Table 1.** Overview of the datasets used in this study.

Variable	Dataset	Spatial resolution	Temporal resolution	Temporal coverage
Surface reflectance (red band and near infrared band)	MCD43C4	0.05 °	daily	2001-2022
Surface reflectance (red band, near infrared band, blue band and shortwave infrared band)	MOD09CMG	0.05 °	daily	2001-2022
LAI	MOD15A2H	500m	8d	2001-2022
FPAR	MOD15A2H	500m	8d	2001-2022
Average air temperature (AT)	ERA5-land	0.1 °	Monthly	2001-2022
Dew point temperature (DPT)	ERA5-land	0.1 °	Monthly	2001-2022
Minimum air temperature (MINT)	ERA5-land	0.1 °	Monthly	2001-2022
Total solar radiation (TSR)	ERA5 monthly data on single levels	0.25 °	Monthly	2001-2022

Direct solar radiation (DirSR)	ERA5 monthly data on single levels	0.25 °	Monthly	2001-2022
CO ₂	NOAA's Earth System Research Laboratory	/	Monthly	2001-2022
Distribution map of C4 crops	Harvested Area and Yield for 175 Crops	1/12 °	Annual	2000
Land use	MCD12C1	0.05 °	Annual	2010

84

85 Previous studies have shown that the photosynthetic capacity of C4 crops is much higher than that of C3 crops (Chen et al.,
86 2014; Chen et al., 2011), so it is necessary to divide the cropland into C3 crops and C4 crops. To estimate the global GPP, we
87 used the dataset "175 Crop harvested Area and yield", which describes the global harvested area and yield of 175 crops in
88 2000 (Monfreda et al., 2008). We extracted the sum of the area ratios of all C4 crops (corn, corn feed, sorghum, sorghum feed,
89 sugarcane, millet) at each grid as the coverage of C4 crops (Figure S1). Consequently, the estimated value of cropland GPP
90 can be expressed as: coverage of C3 crops × simulated GPP value of C3 crops + coverage of C4 crops × simulated GPP value
91 of C4 crops, which was used in a previous study (Guo et al., 2023).

92 The land use map was derived from the IGBP classification of MCD12Q1, and 2010 was chosen as the reference year (that is,
93 land use data is unchanged in the simulation of global GPP). In order to meet the requirements of subsequent research, land
94 cover types were grouped into 9 categories: Deciduous Broadleaf Forest (DBF), Evergreen Needleleaved Forest (ENF),
95 Evergreen Broadleaf Forest (EBF), Mixed Forest (MF), Grassland (GRA), Cropland (including CRO-C3 and CRO-C4),
96 Savannah (SAV), Shrub (SHR), Wetland (WET).

97 Finally, for higher resolution data, we gridded the dataset to 0.05 ° by averaging all pixels whose center fell within each 0.05 °
98 grid cell for upscaling. For lower resolution data, we used the nearest neighbor resampling to 0.05 °. In addition, MODIS data
99 were aggregated to a monthly scale to ensure spatio-temporal consistency.

100 2.2 Observation data at the site scale

101 GPP observations were sourced from the FLUXNET 2015 dataset, which includes carbon fluxes and meteorological variables
102 from more than 200 flux sites around the world (Pastorello et al., 2020). GPP cannot be obtained directly from flux sites and
103 usually needs to be obtained by dismantling the Net Ecosystem Exchange. We chose a monthly level GPP based on the
104 nighttime partitioning method and retained only high quality data ($NEE_VUT_REF_QC > 0.8$) for every year, ultimately
105 selecting 170 sites with 10932 monthly values for this study. In addition, we selected monthly average air temperature, total
106 solar radiation and VPD. The site observations do not provide direct solar radiation, so we extracted data from the ERA5

107 covering the flux tower. Monthly minimum air temperature was derived from hourly air temperature. Since some required
 108 model data are not directly available at flux sites, LAI and FPAR were extracted from MOD15A2H (500 m), and surface
 109 reflectance data (red band, near infrared band, blue band and shortwave infrared band) were derived from MCD43A4 (500 m)
 110 and MOD09A1 (500 m). These data are roughly similar to the footprint of the flux site and can represent the land surface of
 111 the site (Chu et al., 2021).

112 2.3 GPP estimation model

113 We selected six independent models to estimate GPP in this study. These models are widely used with few model parameters
 114 and have demonstrated reliable accuracy in previous studies (Zheng et al., 2020; Zhang et al., 2017; Badgley et al., 2017). The
 115 six models are EC-LUE, Revised-EC-LUE, NIRv-based linear model, kNDVI-based linear model, VPM, MODIS. The VPM,
 116 MODIS and EC-LUE are LUE models based on remote sensing data and meteorological data (Yuan et al., 2007; Running et
 117 al., 2004; Xiao et al., 2004). Recently, Zheng et al. (2020) proposed the Revised-EC-LUE model, which divides the canopy
 118 into sunlit and shaded leaves, improving the estimation of global GPP (Zheng et al., 2020). The NIRv and kNDVI are newly
 119 proposed vegetation indices calculated from the red and near-infrared bands of the reflectance spectrum (Badgley et al., 2017;
 120 Camps-Valls et al., 2021). Similar to solar induced chlorophyll fluorescence, they exhibit a linear relationship with GPP and
 121 are considered effective proxies for GPP. Detailed descriptions of all models can be found in Text S1.

122 To reduce uncertainty in GPP estimate from a single model, we used the ERF model, the basic idea of which is to restructure
 123 the simulated values of multiple models. In this study, we directly used the ERF model to establish the relationship between
 124 the GPP simulated by the above six models and GPP observations. In addition, for comparison with the ERF model, we also
 125 used the random forest (RF) method for modeling. In this study, we used average air temperature, minimum air temperature,
 126 VPD, direct solar radiation, diffuse solar radiation, FPAR and LAI to estimate GPP. Both models used the random forest
 127 method, which has been widely used in previous studies of GPP estimate (Jung et al., 2020; Guo et al., 2023). Random forest
 128 is an ensemble learning algorithm that combines the outputs of multiple decision trees to produce a single result, and is
 129 commonly used for classification and regression problems (Belgiu and Drăguț, 2016). In the regression problem, the output
 130 result of each decision tree is a continuous value, and the average of the output results of all decision trees is taken as the final
 131 result. An overview of all models used can be found in Table 2.

132 **Table 2.** Overview of the models used in this study.

ID	Model	Input data	Output
1	EC-LUE	FPAR, VPD, AT, SRAD, CO ₂	GPP _{EC}
2	Revised-EC-LUE	LAI, VPD, AT, DifSR, DirSR, CO ₂	GPP _{REC}
3	kNDVI-GPP	Red band and near infrared band	GPP _{kNDVI}
4	NIRv-GPP	Red band and near infrared band	GPP _{NIRv}
5	VPM	Red band, near infrared band, blue band,	GPP _{VPM}

6	MODIS	shortwave infrared band, AT, SRAD FPAR, SRAD, MINT, VPD	GPP _{MODIS}
7	Random forest model (RF)	LAI, FPAR, AT, MINT, VPD, DifSR, DirSR	GPP _{RF}
8	Ensemble model based on random forest (ERF)	GPP _{EC} , GPP _{REC} , GPP _{kNDVI} , GPP _{NIRv} , GPP _{MODIS} , GPP _{VPM}	GPP _{ERF}

133

134 **2.4 Model parameter calibration and validation**

135 FLUXNET only provides GPP observations and meteorological data, lacking direct measurements for LAI, FPAR, and surface
136 reflectance, so only remote sensing data can be used. Considering the variety of remote sensing data sources, such as MODIS
137 and AVHRR, it is evident that calibrating the same GPP model with different remote sensing data can yield varied parameters.
138 In addition, the number of sites used to calibrate model parameters is also an important influencing factor for model parameters.
139 The original parameters of these models were calibrated with only a limited number of sites (e.g., 95 sites for Revised EC-
140 LUE and 104 for NIRv) (Wang et al., 2021; Zheng et al., 2020). Therefore, to reduce the impact of the uncertainty of model
141 parameters on simulation results, we did not use original parameters and conducted parameter calibration for GPP models
142 across different vegetation types. For EC-LUE, Revised EC-LUE, VPM and MODIS, the Markov chain Monte Carlo method
143 was used to calibrate model parameters. Traditionally, the mean of the posterior distribution of parameters is taken as the
144 optimal value. However, previous studies have indicated that some model parameters are not well constrained when calibrating
145 multiple model parameters (Xu et al., 2006; Wang et al., 2017), so we selected the parameter with the smallest root-mean-
146 square error (RMSE) as the optimal parameter in each iteration. For each vegetation type, we randomly selected 70% of the
147 sites for parameter calibration, and repeated the process 200 times. In order to avoid overfitting, we adopted the mean of the
148 200 calibrated parameters as the final model parameters. Similarly, for the two vegetation index models, we randomly selected
149 70% of the sites in each vegetation type for parameter calibration, peating the process 200 times and using the mean of the 200
150 calibrated parameters as the final model parameters.

151 After obtaining GPP estimates from the six GPP models, we evaluated the simulation performance of the RF model and the
152 ERF model respectively. For both models, we evaluated the model performance using 5-fold cross-validation, where the
153 process was repeated 200 times, and the mean of the 200 GPP estimates was considered the final GPP estimate. We utilized
154 the determination coefficient (R^2) and RMSE as metrics to evaluate the simulation performance of all models. Additionally,
155 we used the ratio of GPP simulations to GPP observations (Sim/Obs) to measure whether the model overestimates or
156 underestimates.

157 **2.5 Global GPP estimation based on ERF model and its uncertainty.**

158 Based on the ERF model, we estimated global GPP for 2001-2022 (ERF_GPP). The uncertainties of ERF_GPP can be
159 attributed to two primary factors, one is the influence of the number of GPP observations, and the other is the influence of the

160 number of features (that is, the simulated GPP). For the first type of uncertainty, we randomly selected 80% of the data to build
161 a model and simulate the multi-year average of global GPP. The process was repeated 100 times, yielding 100 sets of multi-
162 year averages of ERF_GPP. Their standard deviations were considered as the uncertainty of ERF_GPP caused by the number
163 of GPP observations. For the second type of uncertainty, we selected different number of features to build a model and simulate
164 the multi-year average of global GPP. A total of 56 sets of multi-year averages for ERF_GPP were obtained. The standard
165 deviation of different combinations was considered to be the uncertainty of ERF_GPP caused by the number of features.

166 **2.6 Evaluation of the generalization of different GPP datasets**

167 The majority of flux sites in FLUXNET are concentrated in Europe and North America, it is unclear whether the different GPP
168 estimation methods are suitable for regions with sparse flux sites. Recently, ChinaFlux has published GPP observations from
169 several sites, offering an opportunity to evaluate the generalization of different GPP datasets. However, the spatial resolution
170 of most GPP datasets is 0.05° , and a direct comparison with GPP observations at flux sites is challenging. Therefore, we
171 extracted 0.05° MODIS land use covering the flux sites. If the vegetation type of the flux site matched the MODIS land use,
172 the site was used for the analysis. Finally, a total of 12 flux sites were selected (Figure S2), and Table S1 shows the information
173 of these sites. The same procedure was applied to FLUXNET, resulting in the selection of 52 sites (Figure S2). It should be
174 noted that due to the absence of meteorological data from some sites in Chinaflux, we did not validate all GPP models at the
175 site scale (500 m).

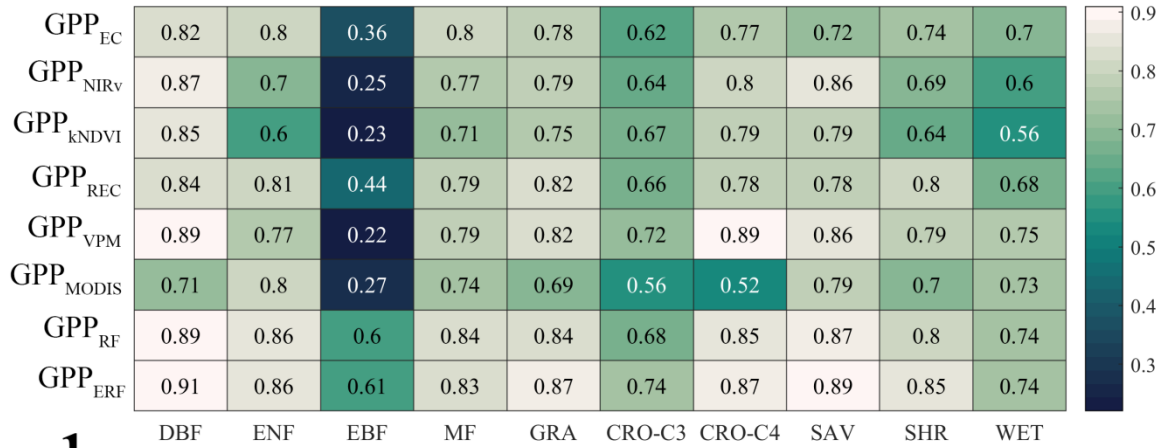
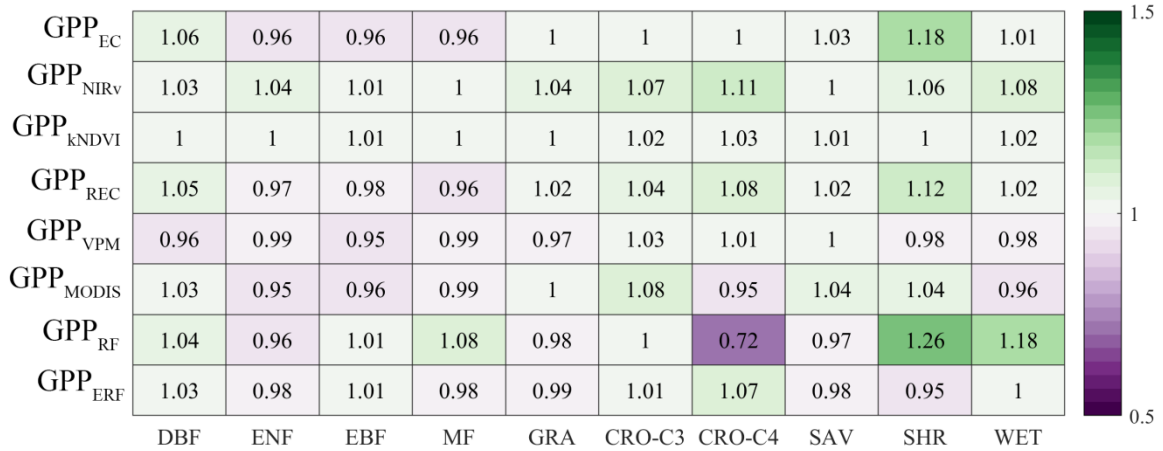
176 We evaluated the generalization of ERF_GPP at 12 ChinaFlux sites and 52 FLUXNET sites. In addition, we selected a number
177 of widely used GPP datasets for comparison, including BESS (Li et al., 2023), GOSIF (Li and Xiao, 2019), FLUXCOM (Jung
178 et al., 2020), NIRv (Wang et al., 2021), Revise-EC-LUE (Zheng et al., 2020), MODIS (Running et al., 2004), VPM (Zhang et
179 al., 2017), which were generated using different GPP estimation methods. These GPP datasets all have a spatial resolution of
180 500 m- 0.5° , similar to the resampling process in section 2.1, we have unified them to 0.05° . The common time range for these
181 datasets spanned from 2001 to 2018, and the temporal resolution was unified to monthly to match the GPP observations.

182 **3 Result**

183 **3.1 Performance of GPP models at site scale**

184 Table S2-S7 show the optimization results of six GPP model parameters. Consistent with the previous study, in the Revised
185 EC-LUE model, the light use efficiency parameter of shade leaves was significantly higher than that of sunlit leaves (Zheng
186 et al., 2020). It is necessary to divide the cropland into C3 crops and C4 crops. In all models, the light use efficiency parameters
187 of C4 crops were significantly higher than those of C3 crops, which was particularly reflected in the two vegetation index
188 models of GPP_{kNDVI} and GPP_{NIRv} , the slope of the linear regression directly reflected the difference in the photosynthetic
189 capacity of the different crops.

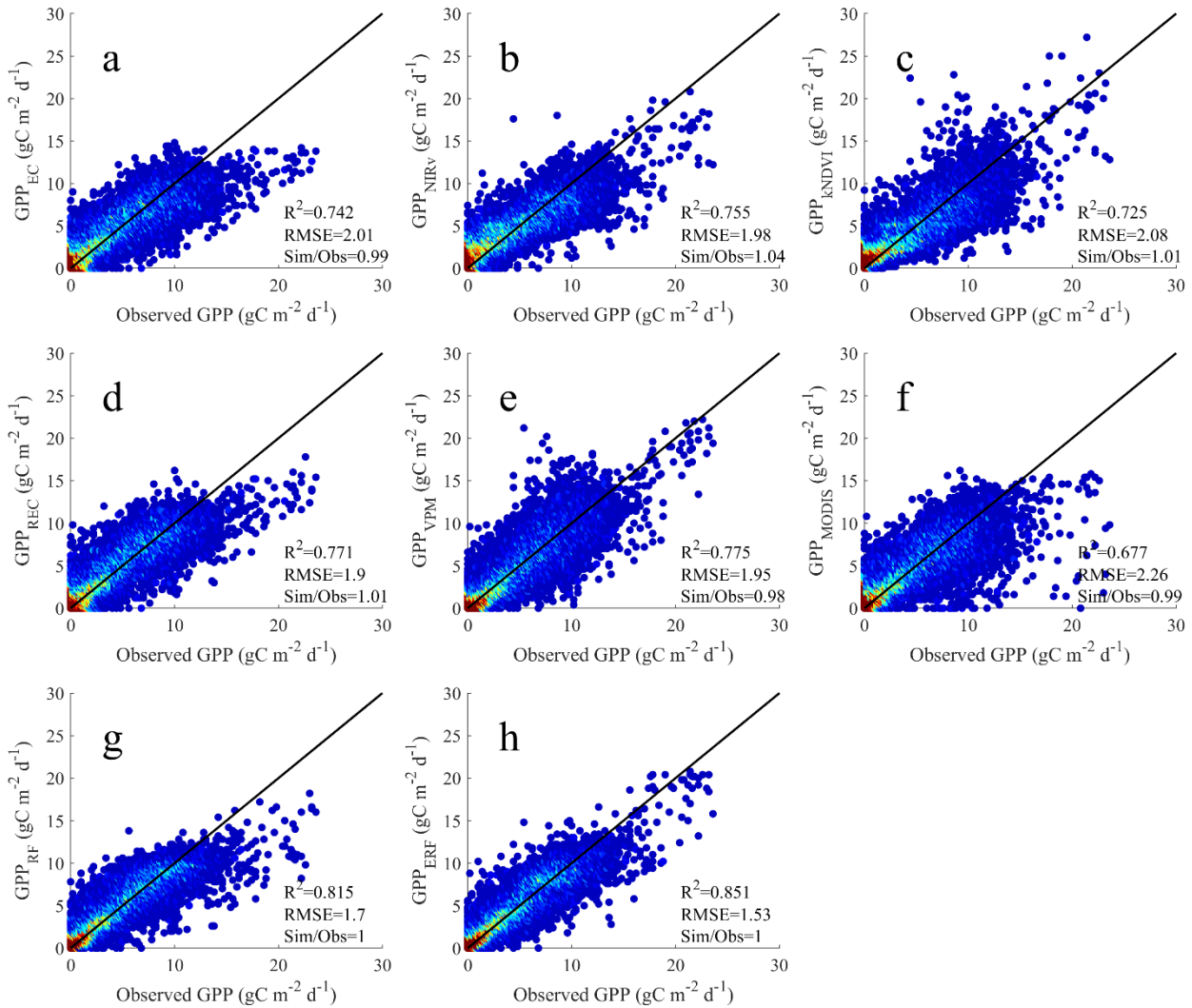
190 Figure 1 shows the performance of all models across different vegetation types. Overall, the performance of the ERF model
191 was better than that of the GPP models. GPP_{ERF} had the higher accuracy among all models, with R^2 between 0.61-0.91 and
192 RMSE between 0.72-2.78 $gC\ m^{-2}\ d^{-1}$. In contrast, the LUE and vegetation index models performed relatively poorly in EBF,
193 with R^2 below 0.5. It is worth noting that compared to other vegetation types, the RMSE was highest for cropland, with 6 out
194 of 8 models for C4 crop exceeding 3 $gC\ m^{-2}\ d^{-1}$, suggesting that these existing GPP models may not properly capture the
195 seasonal changes in cropland GPP. Six models with calibration parameters and ERF model were found to have no significant
196 deviation across vegetation types. However, GPP_{RF} was significantly underestimated for C4 crops and overestimated for SHR.

a**b****c**

198 **Figure 1.** The performance of the eight models on different vegetation types. a, b and c represent R^2 , RMSE, and Sim/Obs respectively.

199 Combining the results of all flux sites, GPP_{ERF} explained 85.1% of the monthly GPP variations, while the seven GPP models
200 only explained 67.7%-81.5% of the monthly GPP variations (Figure 2). In order to further prove the robustness of the ERF
201 model, we also used GPP models with original parameters for modeling and validation. As shown in Figure S3, the
202 performance of these GPP models decreased significantly, with R^2 ranging from 0.570 to 0.719 and RMSE ranging from 2.29
203 to 3.81 $gC\ m^{-2}\ d^{-1}$. The phenomenon of "high underestimation and low overestimation" was also pronounced. However, the
204 ERF model maintained a consistent advantage, with R^2 significantly higher than other GPP models (0.856). In addition, we
205 tested the effect of the amount of GPP on the accuracy of the ERF model. As shown in Table S8, as the number of GPP in the
206 ERF model increased, the performance gain of the model gradually decreased.

207 In summary, GPP_{ERF} showed high accuracy in terms of vegetation type and the ability to interpret monthly variations in GPP,
208 which also illustrates the potential of ERF model to improve GPP estimation. However, it was observed that most GPP
209 simulations exhibited the phenomenon of "high value underestimation and low value overestimation". For example, GPP_{EC} ,
210 GPP_{REC} , GPP_{MODIS} and GPP_{RF} showed obvious underestimation in the months when the monthly GPP value surpassed 15 gC
211 $m^{-2}\ d^{-1}$ (Figure 2). Therefore, it is necessary to evaluate the performance of different models in each month and different
212 subvalues.



213

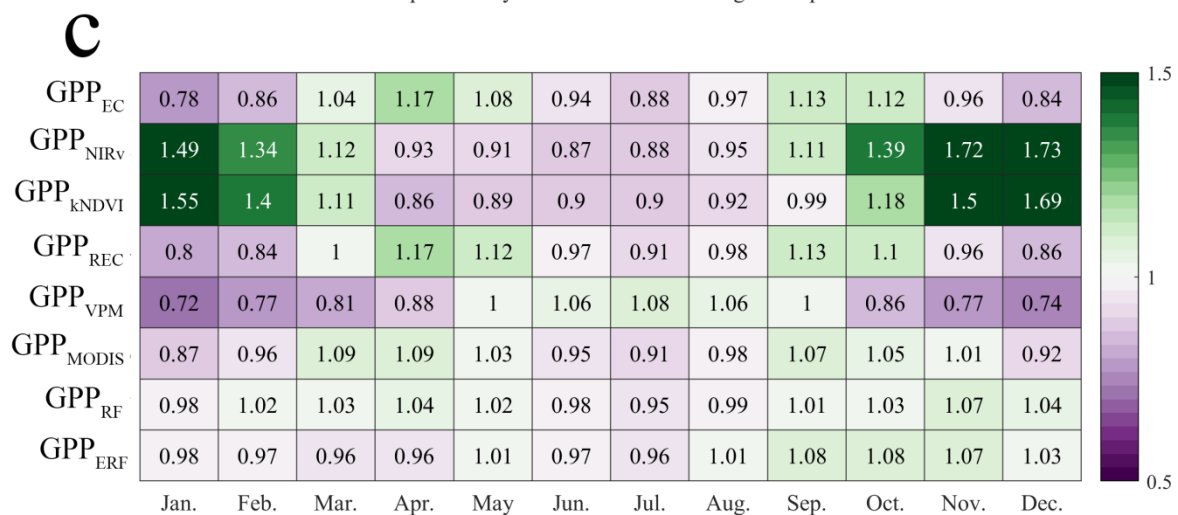
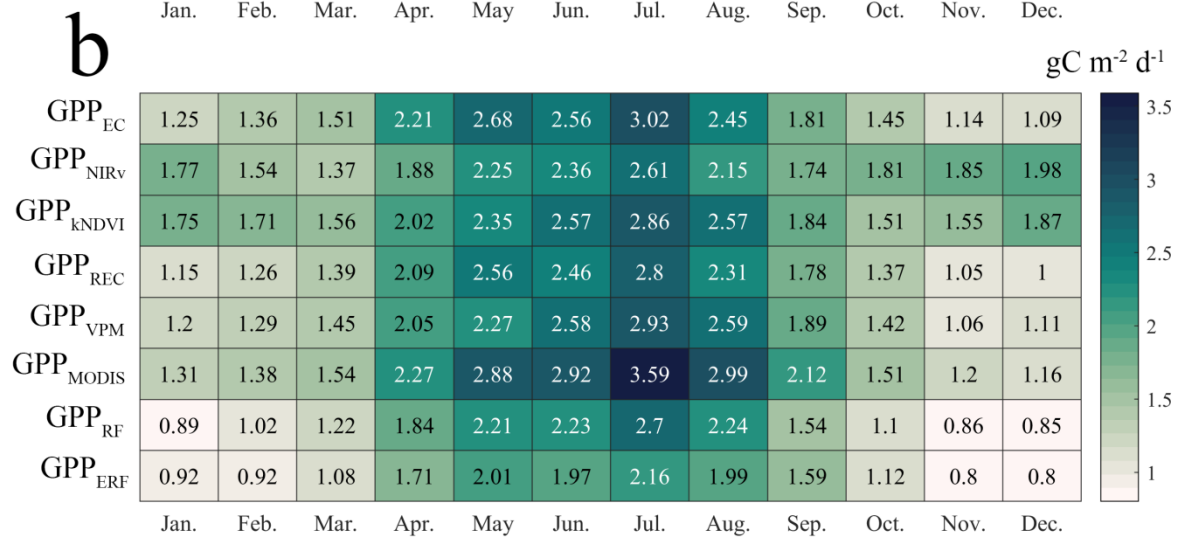
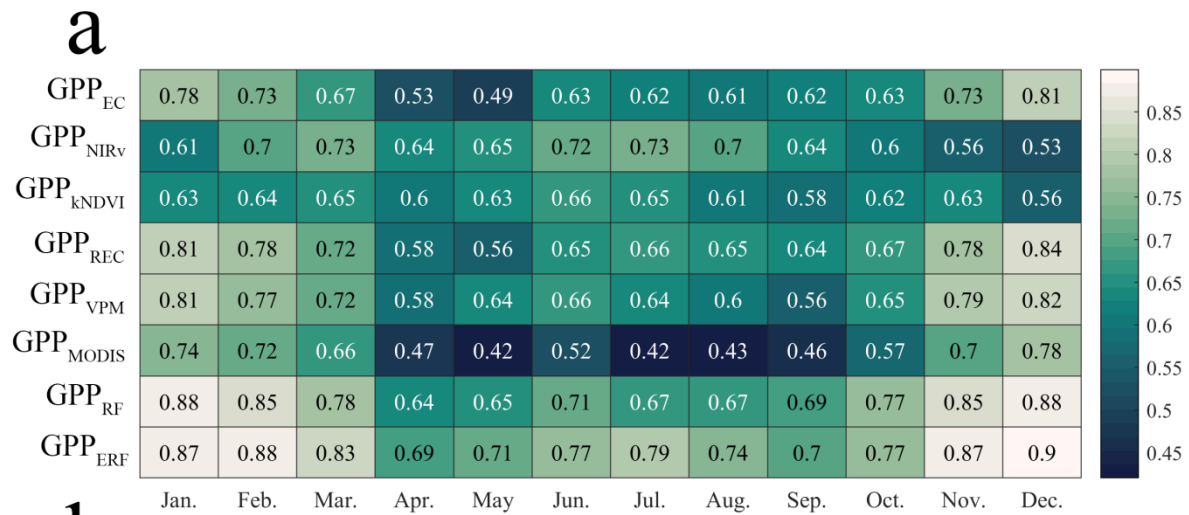
214 **Figure 2.** Comparison between the GPP simulations of the eight models and the GPP observations. a-h represents GPP_{EC} , GPP_{NIRv} , GPP_{KNDVI} ,
 215 GPP_{REC} , GPP_{VPM} , GPP_{MODIS} , GPP_{RF} , GPP_{ERF} , respectively.

216

217 3.2 Performance of GPP models in each month and different subvalues

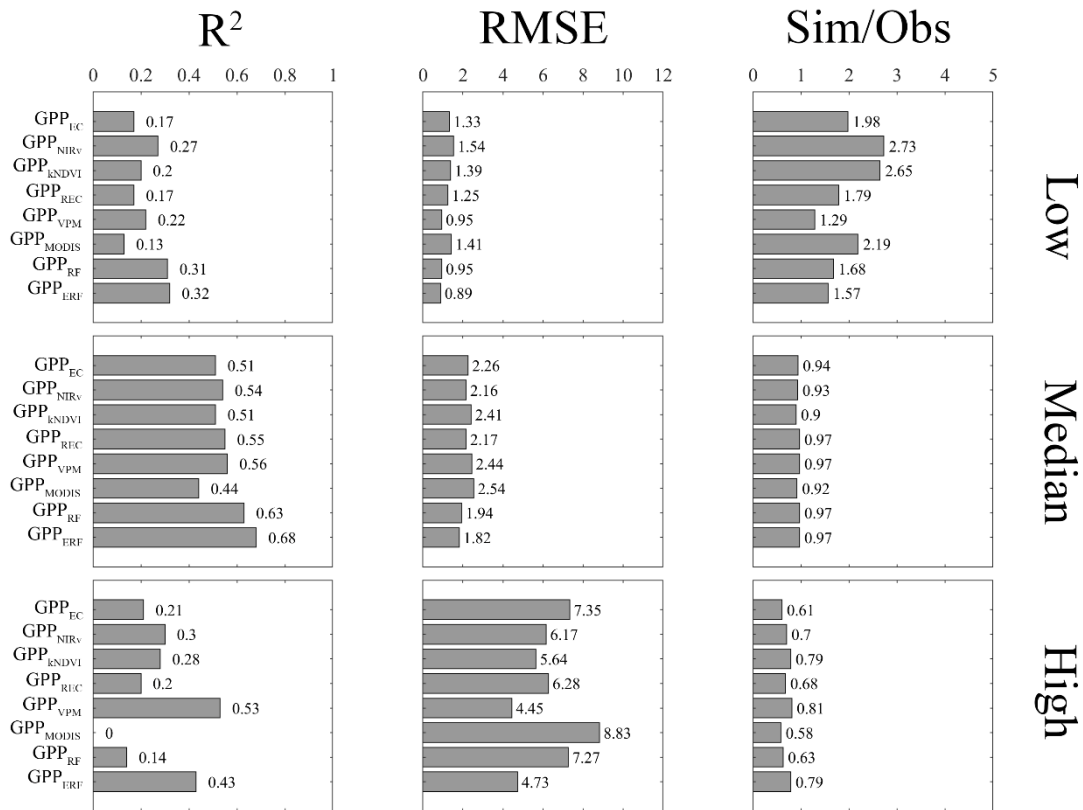
218 Figure 3 shows the simulation accuracy of the eight models in each month. The ERF model maintained a higher accuracy than
 219 other GPP models, with GPP_{ERF} consistently achieving higher R^2 and lower RMSE in most months, and no evident instances
 220 of "high value underestimation and low value overestimation". In contrast, the accuracy of other GPP models was less
 221 satisfactory accuracy, especially during winter (most flux sites are concentrated in the Northern Hemisphere), the LUE models

222 tended to underestimate GPP, and the Sim/Obs remained at 0.72-1.01, although R^2 values were above 0.7. Meanwhile, the
223 vegetation index models overestimated GPP, Sim/Obs remained at 1.34-1.73, and R^2 values were relatively low, mostly around
224 0.6.



226 **Figure 3.** Performance of the eight models in each month. a, b and c represent R^2 , RMSE, and Sim/Obs respectively.

227 We compared the performance of all models in different subvalues, including high value ($GPP > 15 \text{ gC m}^{-2} \text{ d}^{-1}$), median value
 228 ($15 \text{ gC m}^{-2} \text{ d}^{-1} > GPP > 2 \text{ gC m}^{-2} \text{ d}^{-1}$), low value ($GPP < 2 \text{ gC m}^{-2} \text{ d}^{-1}$). For extreme values, most models performed poorly
 229 (Figure 4), with R^2 for GPP models falling below 0.3, and only GPP_{VPM} showing better performance in the high-value range.
 230 GPP_{ERF} demonstrated some improvement in both low and high values, with R^2 0.32 and 0.43, RMSE of 0.89 and 4.73 gC m^{-2}
 231 d^{-1} , and Sim/Obs closer to 1, respectively. In the median value range, all models performed well, with no significant bias in
 232 the GPP estimation. The R^2 of GPP models ranged from 0.44 to 0.68, and the RMSE remained between 1.82 and 2.54 gC m^{-2}
 233 d^{-1} . Further analysis was made at two typical sites, it was obvious that GPP_{EC} , GPP_{REC} and GPP_{MODIS} on CN-Qia exhibited
 234 obvious underestimation during the growing season (Figure S4). On CH_Lae, GPP_{KNDVI} and GPP_{VPM} were significantly
 235 overestimated (Figure S5). In contrast, at both sites, GPP_{ERF} was more consistent with observations, indicating that the superior
 236 performance of GPP_{ERF} was due to the correction on the time series (although not perfectly corrected at all sites).



237

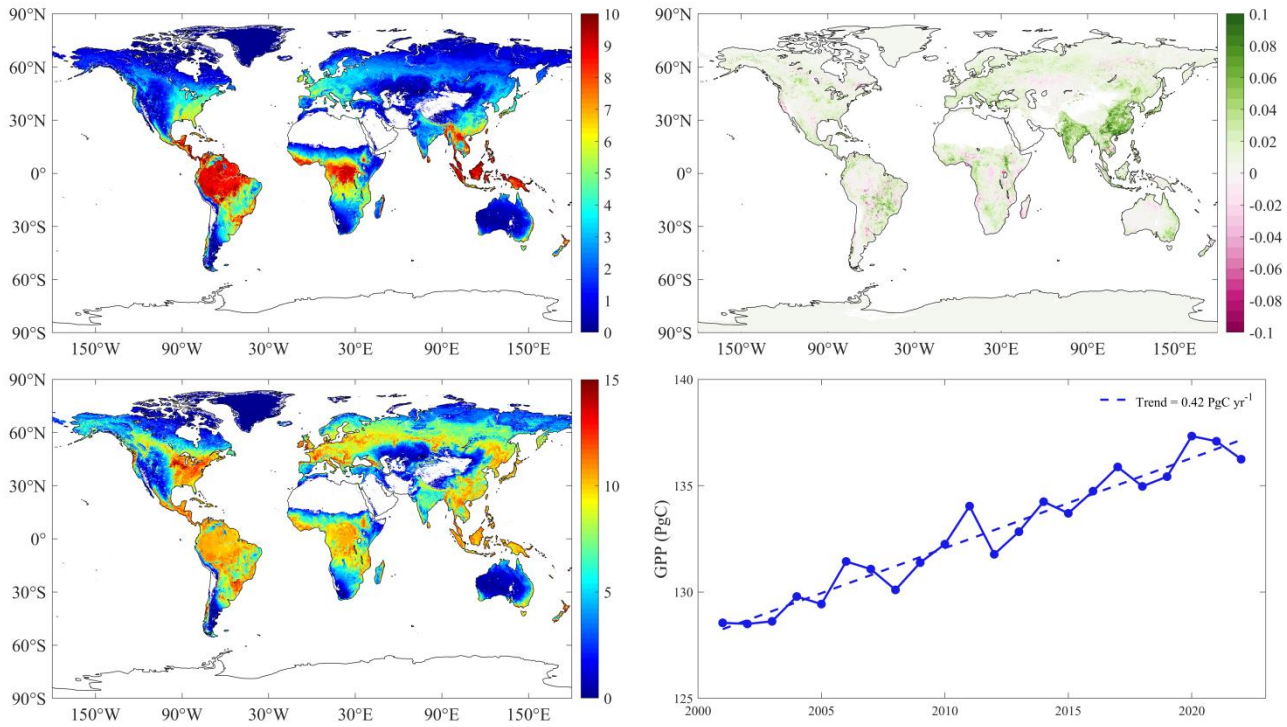
238 **Figure 4.** Performance of eight models in different subvalues.

239 3.3 Temporal and spatial characteristics of ERF_GPP and its generalization evaluation

240 Figure 5a shows the spatial distribution of the multi-year average of ERF_GPP. The high value of GPP was mainly
241 concentrated in tropical areas, exceeding $10 \text{ gC m}^{-2} \text{ d}^{-1}$, and relatively high in southeastern North America, Europe and southern
242 China, about $4\text{-}6 \text{ gC m}^{-2} \text{ d}^{-1}$. From 2001-2022, China and India showed the fastest increase in GPP, mostly at $0.1 \text{ gC m}^{-2} \text{ d}^{-1}$
243 (Figure 5b), similar to a previous study that reported that China and India led the global greening (Chen et al., 2019). We
244 further investigated the annual maximum GPP, as shown in Figure 5c, and the North American corn belt was the global leader
245 in GPP at more than $15 \text{ gC m}^{-2} \text{ d}^{-1}$, compared to only $10 \text{ gC m}^{-2} \text{ d}^{-1}$ in most tropical forests. In 2001-2022, the global GPP was
246 $132.7 \pm 2.8 \text{ PgC yr}^{-1}$, with a trend of 0.42 PgC yr^{-2} . The lowest value was $128.6 \text{ PgC yr}^{-1}$ in 2001, and the highest value was
247 $136.2 \text{ PgC yr}^{-1}$ in 2020 (Figure 5d).

248 The results of the two uncertainty analyses consistently indicated that ERF_GPP exhibited a high uncertainty in tropical regions
249 (Figures S6 and S7), and the uncertainty of ERF_GPP caused by the number of GPP observations was relatively small, the
250 standard deviation of 100 simulations was about $0.3 \text{ gC m}^{-2} \text{ d}^{-1}$ in the tropics and lower in other regions, below $0.1 \text{ gC m}^{-2} \text{ d}^{-1}$.
251 In contrast, the ERF_GPP caused by the number of features was much more uncertain, especially when the number of features
252 was small. It is worth noting that when the number of features was 5, the uncertainty was already substantially less, and the
253 standard deviation was generally lower than $0.5 \text{ gC m}^{-2} \text{ d}^{-1}$.

254



255

256 **Figure 5.** Spatial distribution and interannual change of ERF_GPP during 2001-2022. a represents the multi-year average, b represents the
257 trend, c represents the annual maximum, and d represents the interannual change of GPP.

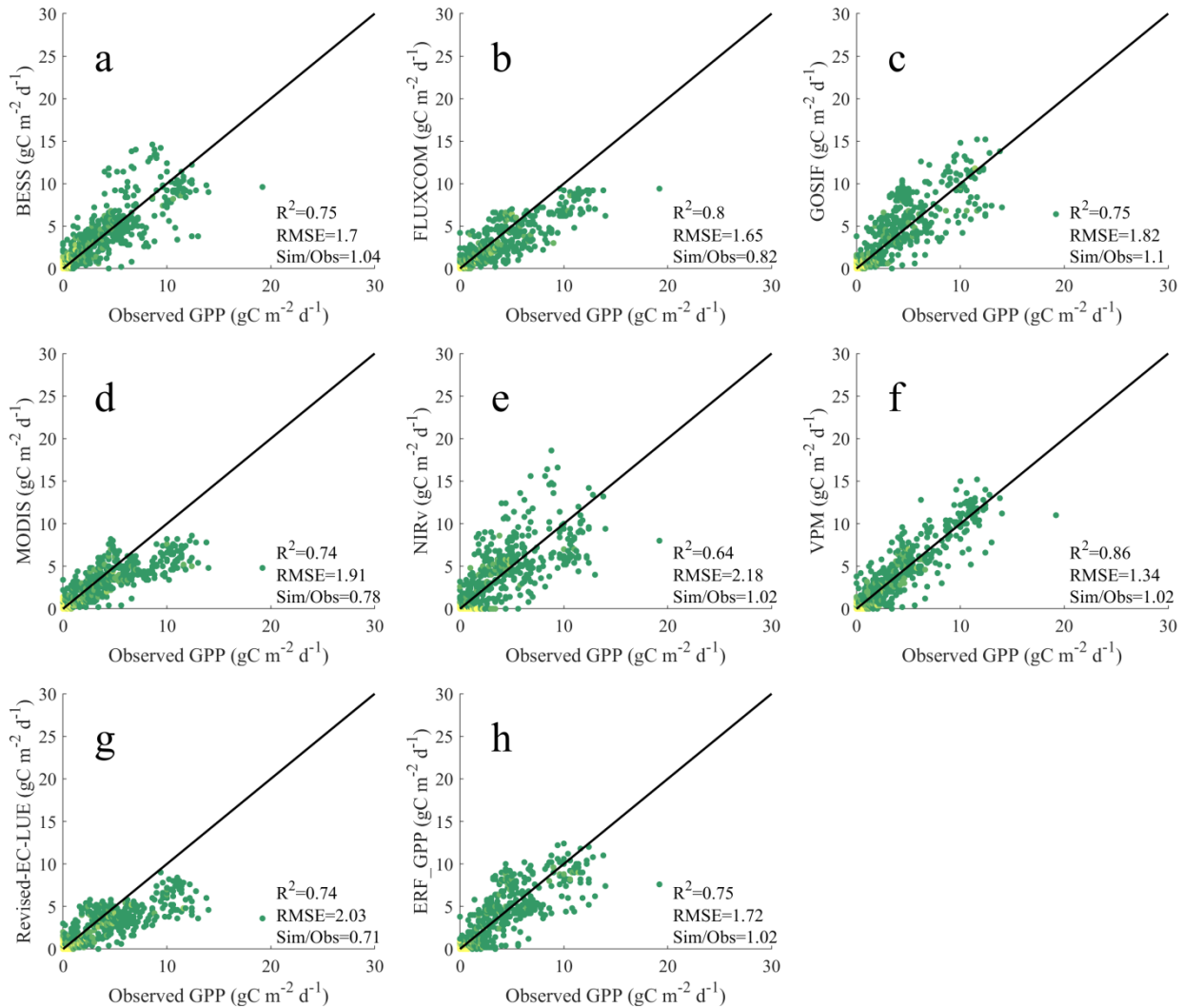
258

259 As shown in Figure 6, ERF_GPP and other GPP datasets were validated using GPP observations from ChinaFlux. Among all
260 the models, GPP_{VPM} demonstrated the best performance, with R^2 of 0.86 and RMSE of $1.34 \text{ gC m}^{-2} \text{ d}^{-1}$. ERF_GPP also
261 exhibited high generalization, with R^2 of 0.75, RMSE of $1.72 \text{ gC m}^{-2} \text{ d}^{-1}$, there was no “high value underestimation and low
262 value overestimation”, which was comparable to the accuracy of BESS and GOSIF. However, the simulation accuracy of the
263 other GPP datasets in Chinaflux was relatively poor, with the R^2 of NIRv being only 0.64, while FLUXCOM, MODIS and
264 Revised EC-LUE were significantly underestimated, with the Sim/Obs being only 0.71-0.82. In the validation of FLUXNET,
265 the R^2 of FLUXCOM, MODIS, and Revised EC-LUE ranged from 0.57 to 0.67, and the RMSE ranged from 2.67 to $3.3 \text{ gC m}^{-2} \text{ d}^{-1}$,
266 and exhibited different degrees of underestimation (Figure S8). Other GPP datasets demonstrated similar performance,
267 with ERF_GPP being the best ($R^2 = 0.74$, $RMSE = 2.26 \text{ gC m}^{-2} \text{ d}^{-1}$).

268

269

270



271

272 **Figure 6.** Comparison between the GPP datasets and the GPP observations from ChinaFlux. a-h represents BESS, FLUXCOM, GOSIF,
 273 MODIS, NIRv, VPM, Revise-EC-LUE, ERF_GPP, respectively.

274 4 Discussion

275 4.1 Performance analysis of different models

276 After parameter calibration, both LUE and vegetation index models obtained reliable model accuracy. However, noticeable
 277 errors persist in different months and subvalues, indicating the prevalent phenomenon of "high value underestimation and low
 278 value overestimation". (Figures 1-4). In addition to MODIS, the GPP simulated by the other three LUE models is generally
 279 underestimated in winter (Figure 3), which may be caused by biases in the parameters used in the meteorological constraints.

280 In the expression form of the temperature constraint adopted by the LUE models, the maximum temperature, minimum
281 temperature and optimum temperature for limiting photosynthesis are all constants, however these values may not be fixed
282 (Huang et al., 2019; Grossiord et al., 2020). A previous study has demonstrated that the GPP estimation could be effectively
283 improved by using dynamic temperature parameters (Chang et al., 2021). Moreover, the form of meteorological constraint is
284 also an important influencing factor. Compared with other LUE models, VPM does not use VPD constraints, but incorporates
285 land surface water index from satellite observations as constraints (Xiao et al., 2004), which may be the reason why the model
286 performs better than other models at high values. Conversely, the two vegetation index models overestimated GPP in winter,
287 and even overestimated by 70% in December. The vegetation index model does not consider meteorological constraints that
288 believe that all environmental impacts on vegetation have been included in the vegetation index (kNDVI, NIRv). However, it
289 is a fact that under high temperatures or low radiation, the vegetation index may still maintain the appearance of high
290 photosynthesis (greening), while in fact the GPP is low (Doughty et al., 2021; Yang et al., 2018; Chen et al., 2024). Furthermore,
291 the relationship between these vegetation indices and GPP is not robust, and the vegetation indices based on reflectance may
292 have hysteresis (Wang et al., 2022).

293 Compared to other GPP models, the ERF model demonstrated better performance ($R^2 = 851$). Since there are no physical
294 constraints, the machine learning model needs to find the relationship between explanatory variables and target variable from
295 a large amount of training data (such as $GPP=f(LAI,T,P, \text{etc.})$). Therefore, the reliability of the model usually depends on the
296 representativeness of the training data. For example, LAI can explain GPP to a large extent, while complex modeling
297 relationships are still needed from LAI to GPP. The difference between the ERF model and the RF model lies in the explanatory
298 variables. The ERF model leverages multiple GPP simulations that are more representative and aligned with the target variable,
299 thus making the GPP simulations more accurate. In other words, the ERF model does not need to take into account the
300 uncertainties of the model structure (such as meteorological constraints) and model parameters (such as maximum light use
301 efficiency), but rather focuses on the uncertainties inherent in the simulated GPP. To further clarify the impact of explanatory
302 variables on the ERF model, we conducted a feature importance analysis (Figure S9). From an average of 200 times, the results
303 of the ERF model did not depend on a single GPP simulation. Even GPP_{MODIS} , with the highest relative importance, accounted
304 for no more than 25%, suggesting that the ERF model behaves more like a weighted average of multiple GPP simulations.

305 It is worth noting that in the study of Tian et al. (2023), the ERF model was also used to improve the GPP estimation. Our
306 research extends this work in several ways. Firstly, parameter calibration was carried out in our study so that the final validation
307 results are comparable, that is, differences in model performance are mainly due to the uncertainty of the model structure.
308 Secondly, our study focuses on the phenomenon of "high value underestimation and low value overestimation" of GPP model,
309 with results indicating that the ERF model performed well across various vegetation types, months, and subvalues. Finally, we
310 generated the ERF_GPP dataset and validate it on different observational datasets, further confirming the robustness of the
311 ERF model in GPP estimation.

312 **4.2 Robustness of ERF_GPP**

313 In this study, based on site-scale validation, we demonstrate the reliability of the ERF model in GPP estimation. However,
314 further discussion is needed regarding the robustness of the spatial distribution, spatial trends and global totals of ERF_GPP.
315 Since the current GPP datasets are generated based on remote sensing observation, there is a strong similarity in spatial
316 distribution among all GPP datasets. Therefore, the validation of GPP observations independent of FLUXNET is crucial.
317 Validation results from GPP observations of ChinaFlux indicated that GPP_{ERF} exhibited good generalization in China
318 ($R^2=0.75$), which was slightly lower than the accuracy of 5-fold-cross-validation during modeling, possibly due to the
319 mismatch between the 0.05° GPP and the footprint of the flux tower (Chu et al., 2021). In addition, the validation of FLUXNET
320 further confirms the reliability of ERF_GPP. Overall, this is comparable to or slightly better than the simulation accuracy of
321 current mainstream GPP datasets. We also observed a clear improvement in the spatial maximum value of ERF_GPP in some
322 corn growing regions, such as the North American Corn Belt (Figure 5c), which is supported by previous studies showing that
323 C4 crops have much higher GPP peaks than other vegetation types (Yuan et al., 2015; Chen et al., 2011).
324 Due to the drought trend, the constraining effect of water on vegetation is gradually increasing, and some studies have reported
325 the decoupling phenomenon of LAI and GPP under some specific conditions (Jiao et al., 2021; Hu et al., 2022). However, in
326 China and India that two regions with significant greening, GPP continues to increase in most datasets, and ERF_GPP supports
327 this view. This phenomenon may be due to the low drought pressure on croplands in China and India due to irrigation, which
328 poses less constraint on GPP (Ambika and Mishra, 2020; Ai et al., 2020). The global estimate of ERF_GPP is 132.7 ± 2.8 PgC
329 yr^{-1} , which is close to estimates from most previous studies (Wang et al., 2021; Badgley et al., 2019). A study have suggested
330 that the global GPP may reach 150-175 PgC yr^{-1} (Welp et al., 2011), however, there is no further evidence to support this view.
331 ERF_GPP exhibited high uncertainty in tropical regions, similar reports have been made in previously published GPP datasets
332 (Badgley et al., 2019; Guo et al., 2023). The scarcity of flux observations in these regions (Pastorello et al., 2020), coupled
333 with the well-known issue of cloud pollution and saturation in remote sensing data in the tropics (Badgley et al., 2019),
334 exacerbates the uncertainty in GPP estimates for these regions. Therefore, in future studies, on the one hand, more flux
335 observations in tropical regions are needed, and on the other hand, attempts can be made to combine optical and microwave
336 data to improve the estimation of GPP.

337 **4.3 Limitations and uncertainties**

338 In this study, we improved GPP estimation based on the ERF model. However, there are still some limitations and uncertainties
339 due to the availability of data and methods. First, C4 crop distribution maps were used in our study to improve estimates of
340 cropland GPP. However, it is important to note that this dataset only represents the spatial distribution of crops around the year
341 2000, which may add uncertainty to GPP simulations of cropland in a few C3 and C4 alternating areas. Secondly, the ERF
342 model considers six GPP simulations, and it is not clear whether adding more GPP simulations to the model can further improve
343 the GPP estimation. Finally, our model did not consider the effect of soil moisture on GPP, and some previous studies have

344 highlighted the importance of incorporating soil moisture in GPP estimates, especially for dry years (Stocker et al., 2019;
345 Stocker et al., 2018).

346 **5 Conclusion**

347 In this study, we compared the performance of the ERF model with other GPP models at the site scale, especially for the
348 phenomenon of "high value underestimation and low value overestimation", and further developed the ERF_GPP dataset.
349 Overall, GPP_{ERF} had higher model accuracy, explaining 85.1% of the monthly GPP variations, and demonstrated reliable
350 accuracy in different months, vegetation types and subvalues. Over the period from 2001 to 2022, the global estimate of
351 ERF_GPP was $132.7 \pm 2.8 \text{ PgC yr}^{-1}$, corresponding to a trend of 0.42 PgC yr^{-2} . Validation results from ChinaFlux indicated
352 that ERF_GPP had good generalization. For the current emerging GPP estimation models, ERF model provides an alternative
353 GPP estimation method that lead to better model accuracy.

354 **Data and code availability**

355 The ERF_GPP for 2001-2022 is available at <https://doi.org/10.6084/m9.figshare.24417649> (Chen et al., 2023). The spatial
356 resolution of ERF_GPP is 0.05° and the temporal resolution is monthly. Code is available from the author upon reasonable
357 request.

358 **Author contributions**

359 X.C. and T.X.C. conceived the scientific ideas and designed this research framework. X.C. compiled the data, conducted
360 analysis, prepared figures. X.C., T.X.C. and Y.F.C. wrote the manuscript. D.X.L., R.J.G., J.D., and S.J.Z. gave constructive
361 suggestions for improving the manuscript.

362 **Acknowledgments**

363 This study was supported by the National Natural Science Foundation of China (No. 42130506, 42161144003 and 31570464)
364 and the Postgraduate Research & Practice Innovation Program of Jiangsu Province (No. KYCX23_1322).

365 **Declaration of interests**

366 The authors have not disclosed any competing interests.

- 368 Ai, Z., Wang, Q., Yang, Y., Manevski, K., Yi, S., and Zhao, X.: Variation of gross primary production, evapotranspiration and
369 water use efficiency for global croplands, *Agricultural and Forest Meteorology*, 287, 10.1016/j.agrformet.2020.107935, 2020.
- 370 Ambika, A. K. and Mishra, V.: Substantial decline in atmospheric aridity due to irrigation in India, *Environmental Research*
371 *Letters*, 15, 10.1088/1748-9326/abc8bc, 2020.
- 372 Anav, A., Friedlingstein, P., Beer, C., Ciais, P., Harper, A., Jones, C., Murray-Tortarolo, G., Papale, D., Parazoo, N. C., Peylin,
373 P., Piao, S., Sitch, S., Viovy, N., Wiltshire, A., and Zhao, M.: Spatiotemporal patterns of terrestrial gross primary production:
374 A review, *Reviews of Geophysics*, 53, 785-818, 10.1002/2015rg000483, 2015.
- 375 Badgley, G., Field, C. B., and Berry, J. A.: Canopy near-infrared reflectance and terrestrial photosynthesis, *Science advances*,
376 3, e1602244, 2017.
- 377 Badgley, G., Anderegg, L. D., Berry, J. A., and Field, C. B.: Terrestrial gross primary production: Using NIRV to scale from
378 site to globe, *Global change biology*, 25, 3731-3740, 2019.
- 379 Bai, Y., Zhang, S., Bhattarai, N., Mallick, K., Liu, Q., Tang, L., Im, J., Guo, L., and Zhang, J.: On the use of machine learning
380 based ensemble approaches to improve evapotranspiration estimates from croplands across a wide environmental gradient,
381 *Agricultural and Forest Meteorology*, 298, 108308, 2021.
- 382 Belgiu, M. and Drăguț, L.: Random forest in remote sensing: A review of applications and future directions, *ISPRS journal of*
383 *photogrammetry and remote sensing*, 114, 24-31, 2016.
- 384 Camps-Valls, G., Campos-Taberner, M., Moreno-Martínez, Á., Walther, S., Duveiller, G., Cescatti, A., Mahecha, M. D.,
385 Muñoz-Marí J., García-Haro, F. J., and Guanter, L.: A unified vegetation index for quantifying the terrestrial biosphere,
386 *Science Advances*, 7, eabc7447, 2021.
- 387 Chang, Q., Xiao, X. M., Doughty, R., Wu, X. C., Jiao, W. Z., and Qin, Y. W.: Assessing variability of optimum air temperature
388 for photosynthesis across site-years, sites and biomes and their effects on photosynthesis estimation, *Agricultural and Forest*
389 *Meteorology*, 298, 10.1016/j.agrformet.2020.108277, 2021.
- 390 Chen, C., Park, T., Wang, X., Piao, S., Xu, B., Chaturvedi, R. K., Fuchs, R., Brovkin, V., Ciais, P., Fensholt, R., Tommervik,
391 H., Bala, G., Zhu, Z., Nemani, R. R., and Myneni, R. B.: China and India lead in greening of the world through land-use
392 management, *Nature Sustainability*, 2, 122-129, 10.1038/s41893-019-0220-7, 2019.
- 393 Chen, X., Chen, T., Li, X., Chai, Y., Zhou, S., Guo, R., Dai, J.: 2001-2022 global gross primary productivity dataset using an
394 ensemble model based on random forest. figshare. Dataset. <https://doi.org/10.6084/m9.figshare.24417649.v2>, 2023
- 395 Chen, T., van der Werf, G. R., Dolman, A. J., and Groenendijk, M.: Evaluation of cropland maximum light use efficiency
396 using eddy flux measurements in North America and Europe, *Geophysical Research Letters*, 38, 10.1029/2011gl047533, 2011.
- 397 Chen, T., Van Der Werf, G., Gobron, N., Moors, E., and Dolman, A.: Global cropland monthly gross primary production in
398 the year 2000, *Biogeosciences*, 11, 3871-3880, 2014.
- 399 Chen, X., Chen, T., Liu, S., Chai, Y., Guo, R., Dai, J., Wang, S., Zhang, L., and Wei, X.: Vegetation Index -Based Models
400 Without Meteorological Constraints Underestimate the Impact of Drought on Gross Primary Productivity, *Journal of*
401 *Geophysical Research: Biogeosciences*, 129, e2023JG007499, 2024.
- 402 Chen, Y., Yuan, H., Yang, Y., and Sun, R.: Sub-daily soil moisture estimate using dynamic Bayesian model averaging, *Journal*
403 *of Hydrology*, 590, 125445, 2020.
- 404 Chu, H., Luo, X., Ouyang, Z., Chan, W. S., Dengel, S., Biraud, S. C., Torn, M. S., Metzger, S., Kumar, J., and Arain, M. A.:
405 Representativeness of Eddy-Covariance flux footprints for areas surrounding AmeriFlux sites, *Agricultural and Forest*
406 *Meteorology*, 301, 108350, 2021.
- 407 Dechant, B., Ryu, Y., Badgley, G., Köhler, P., Rascher, U., Migliavacca, M., Zhang, Y., Tagliabue, G., Guan, K., and Rossini,
408 M.: NIRVP: A robust structural proxy for sun-induced chlorophyll fluorescence and photosynthesis across scales, *Remote*
409 *Sensing of Environment*, 268, 112763, 2022.
- 410 Dechant, B., Ryu, Y., Badgley, G., Zeng, Y., Berry, J. A., Zhang, Y., Goulas, Y., Li, Z., Zhang, Q., and Kang, M.: Canopy
411 structure explains the relationship between photosynthesis and sun-induced chlorophyll fluorescence in crops, *Remote Sensing*
412 *of Environment*, 241, 111733, 2020.
- 413 Doughty, R., Xiao, X. M., Qin, Y. W., Wu, X. C., Zhang, Y., and Moore, B.: Small anomalies in dry-season greenness and
414 chlorophyll fluorescence for Amazon moist tropical forests during El Niño and La Niña, *Remote Sensing of Environment*, 253,
415 10.1016/j.rse.2020.112196, 2021.

416 Grossiord, C., Buckley, T. N., Cernusak, L. A., Novick, K. A., Poulter, B., Siegwolf, R. T., Sperry, J. S., and McDowell, N.
417 G.: Plant responses to rising vapor pressure deficit, *New Phytologist*, 226, 1550-1566, 2020.

418 Guo, R., Chen, T., Chen, X., Yuan, W., Liu, S., He, B., Li, L., Wang, S., Hu, T., Yan, Q., Wei, X., and Dai, J.: Estimating
419 Global GPP From the Plant Functional Type Perspective Using a Machine Learning Approach, *Journal of Geophysical*
420 *Research-Biogeosciences*, 128, 10.1029/2022jg007100, 2023.

421 Hersbach, H., Bell, B., Berrisford, P., Hirahara, S., Horányi, A., Muñoz-Sabater, J., Nicolas, J., Peubey, C., Radu, R., and
422 Schepers, D.: The ERA5 global reanalysis, *Quarterly Journal of the Royal Meteorological Society*, 146, 1999-2049, 2020.

423 Hu, Z., Piao, S., Knapp, A. K., Wang, X., Peng, S., Yuan, W., Running, S., Mao, J., Shi, X., and Ciais, P.: Decoupling of
424 greenness and gross primary productivity as aridity decreases, *Remote Sensing of Environment*, 279, 113120, 2022.

425 Huang, M., Piao, S., Ciais, P., Peñuelas, J., Wang, X., Keenan, T. F., Peng, S., Berry, J. A., Wang, K., and Mao, J.: Air
426 temperature optima of vegetation productivity across global biomes, *Nature ecology & evolution*, 3, 772-779, 2019.

427 Jiao, W., Wang, L., Smith, W. K., Chang, Q., Wang, H., and D'Odorico, P.: Observed increasing water constraint on vegetation
428 growth over the last three decades, *Nature Communications*, 12, 10.1038/s41467-021-24016-9, 2021.

429 Jung, M., Koirala, S., Weber, U., Ichii, K., Gans, F., Camps-Valls, G., Papale, D., Schwalm, C., Tramontana, G., and Reichstein,
430 M.: The FLUXCOM ensemble of global land-atmosphere energy fluxes, *Scientific data*, 6, 1-14, 2019.

431 Jung, M., Schwalm, C., Migliavacca, M., Walther, S., Camps-Valls, G., Koirala, S., Anthoni, P., Besnard, S., Bodesheim, P.,
432 and Carvalhais, N.: Scaling carbon fluxes from eddy covariance sites to globe: synthesis and evaluation of the FLUXCOM
433 approach, *Biogeosciences*, 17, 1343-1365, 2020.

434 Li, B., Ryu, Y., Jiang, C., Dechant, B., Liu, J., Yan, Y., and Li, X.: BESSv2.0: A satellite-based and coupled-process model
435 for quantifying long-term global land-atmosphere fluxes, *Remote Sensing of Environment*, 295, 10.1016/j.rse.2023.113696,
436 2023.

437 Li, X. and Xiao, J.: A Global, 0.05-Degree Product of Solar-Induced Chlorophyll Fluorescence Derived from OCO-2, MODIS,
438 and Reanalysis Data, *Remote Sensing*, 11, 10.3390/rs11050517, 2019.

439 Monfreda, C., Ramankutty, N., and Foley, J. A.: Farming the planet: 2. Geographic distribution of crop areas, yields,
440 physiological types, and net primary production in the year 2000, *Global Biogeochemical Cycles*, 22, 10.1029/2007gb002947,
441 2008.

442 Pastorello, G., Trotta, C., Canfora, E., Chu, H., Christianson, D., Cheah, Y.-W., Poindexter, C., Chen, J., Elbashandy, A., and
443 Humphrey, M.: The FLUXNET2015 dataset and the ONEFlux processing pipeline for eddy covariance data, *Scientific data*,
444 7, 1-27, 2020.

445 Pei, Y., Dong, J., Zhang, Y., Yuan, W., Doughty, R., Yang, J., Zhou, D., Zhang, L., and Xiao, X.: Evolution of light use
446 efficiency models: Improvement, uncertainties, and implications, *Agricultural and Forest Meteorology*, 317, 108905, 2022.

447 Ruehr, S., Keenan, T. F., Williams, C., Zhou, Y., Lu, X., Bastos, A., Canadell, J. G., Prentice, I. C., Sitch, S., and Terrer, C.:
448 Evidence and attribution of the enhanced land carbon sink, *Nature Reviews Earth & Environment*, 4, 518-534,
449 10.1038/s43017-023-00456-3, 2023.

450 Running, S. W., Nemani, R. R., Heinsch, F. A., Zhao, M., Reeves, M., and Hashimoto, H.: A continuous satellite-derived
451 measure of global terrestrial primary production, *Bioscience*, 54, 547-560, 2004.

452 Ryu, Y., Berry, J. A., and Baldocchi, D. D.: What is global photosynthesis? History, uncertainties and opportunities, *Remote*
453 *sensing of environment*, 223, 95-114, 2019.

454 Stocker, B. D., Zscheischler, J., Keenan, T. F., Prentice, I. C., Penuelas, J., and Seneviratne, S. I.: Quantifying soil moisture
455 impacts on light use efficiency across biomes, *New Phytologist*, 218, 1430-1449, 10.1111/nph.15123, 2018.

456 Stocker, B. D., Zscheischler, J., Keenan, T. F., Prentice, I. C., Seneviratne, S. I., and Penuelas, J.: Drought impacts on terrestrial
457 primary production underestimated by satellite monitoring, *Nature Geoscience*, 12, 264-+, 10.1038/s41561-019-0318-6, 2019.

458 Tian, Z., Yi, C., Fu, Y., Kutter, E., Krakauer, N. Y., Fang, W., Zhang, Q., and Luo, H.: Fusion of Multiple Models for
459 Improving Gross Primary Production Estimation With Eddy Covariance Data Based on Machine Learning, *Journal of*
460 *Geophysical Research: Biogeosciences*, 128, e2022JG007122, <https://doi.org/10.1029/2022JG007122>, 2023.

461 Wang, J., Dong, J., Yi, Y., Lu, G., Oyler, J., Smith, W., Zhao, M., Liu, J., and Running, S.: Decreasing net primary production
462 due to drought and slight decreases in solar radiation in China from 2000 to 2012, *Journal of Geophysical Research:*
463 *Biogeosciences*, 122, 261-278, 2017.

464 Wang, S., Zhang, Y., Ju, W., Qiu, B., and Zhang, Z.: Tracking the seasonal and inter-annual variations of global gross primary
465 production during last four decades using satellite near-infrared reflectance data, *Science of the Total Environment*, 755,
466 142569, 2021.

467 Wang, X., Biederman, J. A., Knowles, J. F., Scott, R. L., Turner, A. J., Dannenberg, M. P., Köhler, P., Frankenberg, C., Litvak,
468 M. E., and Flerchinger, G. N.: Satellite solar-induced chlorophyll fluorescence and near-infrared reflectance capture
469 complementary aspects of dryland vegetation productivity dynamics, *Remote Sensing of Environment*, 270, 112858, 2022.

470 Welp, L. R., Keeling, R. F., Meijer, H. A. J., Bollenbacher, A. F., Piper, S. C., Yoshimura, K., Francey, R. J., Allison, C. E.,
471 and Wahlen, M.: Interannual variability in the oxygen isotopes of atmospheric CO₂ driven by El Niño, *Nature*,
472 477, 579-582, 10.1038/nature10421, 2011.

473 Xiao, J., Chevallier, F., Gomez, C., Guanter, L., Hicke, J. A., Huete, A. R., Ichii, K., Ni, W., Pang, Y., and Rahman, A. F.:
474 Remote sensing of the terrestrial carbon cycle: A review of advances over 50 years, *Remote Sensing of Environment*, 233,
475 111383, 2019.

476 Xiao, X., Zhang, Q., Braswell, B., Urbanski, S., Boles, S., Wofsy, S., Moore III, B., and Ojima, D.: Modeling gross primary
477 production of temperate deciduous broadleaf forest using satellite images and climate data, *Remote sensing of environment*,
478 91, 256-270, 2004.

479 Xu, T., White, L., Hui, D., and Luo, Y.: Probabilistic inversion of a terrestrial ecosystem model: Analysis of uncertainty in
480 parameter estimation and model prediction, *Global Biogeochemical Cycles*, 20, 2006.

481 Yang, J., Tian, H. Q., Pan, S. F., Chen, G. S., Zhang, B. W., and Dangal, S.: Amazon drought and forest response: Largely
482 reduced forest photosynthesis but slightly increased canopy greenness during the extreme drought of 2015/2016, *Global
483 Change Biology*, 24, 1919-1934, 10.1111/gcb.14056, 2018.

484 Yao, Y., Liang, S., Li, X., Chen, J., Liu, S., Jia, K., Zhang, X., Xiao, Z., Fisher, J. B., and Mu, Q.: Improving global terrestrial
485 evapotranspiration estimation using support vector machine by integrating three process-based algorithms, *Agricultural and
486 Forest Meteorology*, 242, 55-74, 2017.

487 Yao, Y., Liang, S., Li, X., Hong, Y., Fisher, J. B., Zhang, N., Chen, J., Cheng, J., Zhao, S., and Zhang, X.: Bayesian multimodel
488 estimation of global terrestrial latent heat flux from eddy covariance, meteorological, and satellite observations, *Journal of
489 Geophysical Research: Atmospheres*, 119, 4521-4545, 2014.

490 Yuan, W., Cai, W., Nguy-Robertson, A. L., Fang, H., Suyker, A. E., Chen, Y., Dong, W., Liu, S., and Zhang, H.: Uncertainty
491 in simulating gross primary production of cropland ecosystem from satellite-based models, *Agricultural and Forest
492 Meteorology*, 207, 48-57, 10.1016/j.agrformet.2015.03.016, 2015.

493 Yuan, W., Cai, W., Xia, J., Chen, J., Liu, S., Dong, W., Merbold, L., Law, B., Arain, A., and Beringer, J.: Global comparison
494 of light use efficiency models for simulating terrestrial vegetation gross primary production based on the LaThuile database,
495 *Agricultural and Forest Meteorology*, 192, 108-120, 2014.

496 Yuan, W., Liu, S., Zhou, G., Zhou, G., Tieszen, L. L., Baldocchi, D., Bernhofer, C., Gholz, H., Goldstein, A. H., and Goulden,
497 M. L.: Deriving a light use efficiency model from eddy covariance flux data for predicting daily gross primary production
498 across biomes, *Agricultural and Forest Meteorology*, 143, 189-207, 2007.

499 Yuan, W., Zheng, Y., Piao, S., Ciais, P., Lombardozzi, D., Wang, Y., Ryu, Y., Chen, G., Dong, W., and Hu, Z.: Increased
500 atmospheric vapor pressure deficit reduces global vegetation growth, *Science advances*, 5, eaax1396, 2019.

501 Zhang, Y., Xiao, X., Wu, X., Zhou, S., Zhang, G., Qin, Y., and Dong, J.: A global moderate resolution dataset of gross primary
502 production of vegetation for 2000–2016, *Scientific data*, 4, 1-13, 2017.

503 Zheng, Y., Shen, R., Wang, Y., Li, X., Liu, S., Liang, S., Chen, J. M., Ju, W., Zhang, L., and Yuan, W.: Improved estimate of
504 global gross primary production for reproducing its long-term variation, 1982–2017, *Earth System Science Data*, 12, 2725-
505 2746, 2020.

506

507